

Direct Evidence of a Highest Wave-Driven Energetic Electron Flux at the Earth's Magnetopause

Shubhangi Lagad¹, Amar Kakad^{1,*}, and Bharati Kakad¹

¹Indian Institute of Geomagnetism, New Panvel, Navi Mumbai, 410218, India

*amar.kakad@iigm.res.in

ABSTRACT

Spacecraft observations of high-energy electron flux enhancement up to 125 keV at Earth's magnetopause are typically linked to the magnetic reconnection. Here, we report the first ever observation of prolonged electron flux enhancement reaching very high energy up to 650 keV at magnetopause near the subsolar point, notably without reconnection signatures. The observation reveals that the high-energy electron flux enhancement near the magnetopause is associated with the simultaneous occurrence of electron cyclotron wave harmonics, whistler waves, and Langmuir waves. Theoretical modeling confirms the wave generation by electron temperature anisotropy and the electron loss cone distribution. This direct, in-situ observation of high-energy electron flux linked to cascaded wave-particle interactions will help us advance our understanding about the tiniest electron-scale intricacies affecting near-Earth space weather.

Introduction

The Earth's magnetosphere is an exceptional, naturally occurring plasma laboratory that can be used to study basic plasma processes. The complex interaction between the solar wind and the geomagnetic field, via magnetic reconnection, facilitates the transfer of solar wind mass, momentum, and energy into the magnetosphere^{1,2}. Magnetic reconnection is fundamental in driving various plasma processes³ on the day and nightside of the magnetosphere, impacting the near-Earth space weather. Among these processes, the electron acceleration near the reconnection region has received much attention since the launch of the Magnetospheric Multiscale (MMS) mission. While reconnection at the magnetopause rarely shows strong electron acceleration⁴, magnetotail observations reveal electron acceleration up to 200 - 300 keV^{5,6}. Recent observations demonstrate that the acceleration in the magnetotail can significantly exceed previous estimates, leading to electron populations with energies up to several MeV⁷. Spacecraft observations show that the whistler waves, electron cyclotron waves and their harmonics (ECH), and waves around electron plasma frequency f_{pe} , play a key role in local electron heating, particularly during reconnection as these are high-frequency and localized waves⁸. During magnetotail reconnection, whistler waves are associated with perpendicular heating of few to tens of keV electrons leading to a temperature anisotropy that promotes wave growth⁹. Farrell et al.^{10,11} reported waves around electron plasma frequency during magnetotail reconnection. Whistler waves are often related to the dayside magnetic reconnection¹²⁻¹⁷. Langmuir and ECH are also reported during magnetic reconnection^{10,18}. There are reports about the simultaneous observations of whistler and Langmuir waves¹⁹, and whistler and ECH waves²⁰ during magnetic reconnection.

The solar wind varies on the timescale from less than seconds to hours, causing the magnetopause, where the solar wind interacts with the geomagnetic field, is always in a state of dynamic behaviour. The magnetopause's response to such varying input is rapid and abrupt leading to intensification of plasma waves and high energy fluxes. Jaynes et al.¹² reported electron flux enhancement up to 100 keV and Fu et al.¹³ reported up to 4 keV during magnetic reconnection at the magnetopause. Chepuri et al.¹⁴ reported flux enhancements up to 100 keV from 2016 - 2020 magnetopause crossing events, many of them showing reconnection signatures.

The wave dynamical complexity further increases with intense solar eruptions that cause severe geomagnetic activities. There are several reports about the intensification of the electron waves²¹⁻²⁵ during geomagnetically active times. We are approaching the peak of the 25th solar cycle even before reaching its maximum, a multi-CME generated intense geomagnetic storm; the strongest solar storm of two decades hit the magnetosphere on May 10 - 11, 2024. This event provides an opportunity to study complex plasma intricacies at Earth's magnetopause.

We report here the prolonged high-energy electron flux enhancement up to 650 keV and simultaneous observations of electron cyclotron harmonics, whistler, and Langmuir waves, notably without magnetic reconnection. These observations indicate the direct role of the electron-scale waves in heating the electrons at the magnetopause.

Results

Dataset

We use the data from the Magnetospheric Multiscale (MMS) spacecraft²⁶. Specifically, high-resolution burst mode data is analyzed to study the electron wave dynamics. For three-dimensional electric field measurement, high-frequency AC coupled electric field (HMFE) data from electric field double probes (EDP) is analyzed^{27, 28}. Magnetic field measurements are obtained using Fluxgate Magnetometer (FGM)²⁹ and Search Coil Magnetometer (SCM)³⁰. FGM measures DC magnetic fields at a sampling frequency of 128 Hz, while EDP and SCM sample electric and magnetic field waveforms at 65.536 kHz and 16.384 kHz, respectively. For particle measurements, the data from Fast Plasma Investigation (FPI)³¹ and the Fly's Eye Energetic Electron Proton Spectrometer (FEEPS)³² are used. The sampling frequency of burst mode FPI data is 33.33 Hz whereas, the FEEPS instrument can measure all-sky snapshots (nearly 360°) of electron intensity from ~25 to 650 keV every 0.33 s in burst mode. At this count, the local magnetic field measurements can be used to determine pitch angle distributions at differential energies. To provide an overview of localized magnetospheric parameters, fast and survey mode datasets are used. The burst dataset of the electric field is not available for MMS 4. Other than this all the datasets mentioned above are available for the other three spacecraft. In this paper, the observations of the MMS 3 satellite are shown. The geomagnetic index SYM-H and other interplanetary parameters are obtained from the OMNI dataset.

Prolonged High-Energy Flux Enhancement at the Magnetopause

We report the first ever observation of prolonged high-energy electron flux enhancements up to 650 keV during the MMS's magnetopause crossing, notably without magnetic reconnection signatures. It is also possible that this flux enhancement could exceed 650 keV; however, this cannot be confirmed as the maximum energy coverage limit of the FEEPS instrument is capped at 650 keV. These observations are during the recovery phase of the severe G5 storm which occurred on May 10 - 11, 2024 as shown in the in the Supplementary Figure 1.

On May 11, 2024, at 14:39 UT MMS was situated around [6.1465, -3.0864, -0.0602] R_E , where R_E is the Earth's radius in the GSE coordinate system. The maximum separation between MMS spacecrafts is around 75 km. The trajectory of the MMS spacecraft orbit and their tetrahedral geometry is shown in Supplementary Figure 2. The red dashed lines in the Supplementary Figure 1 mark the timestamps when MMS was positioned near the subsolar point at the magnetopause during the recovery phase of a geomagnetic storm. An overview of the event, the electron measurements including electron density (n_e), velocity components (v_x , v_y , v_z), parallel and perpendicular temperature (T_{\parallel} , T_{\perp}) along with magnetic field components (B_x , B_y , B_z) is shown in Figure 1a-e. The magenta dashed lines in this figure highlight the periods when burst mode data is available. Focusing on this specific region, we observe fluctuations in the magnetospheric magnetic field (Figure 1a), density gradient (Figure 1b), parallel and perpendicular temperature (Figure 1d), temperature anisotropy in the perpendicular direction and its intensification (Figure 1e). These factors may act as a precursor for the generation of electron-scale waves locally.

Figure 1f shows the omnidirectional electron flux and the electron flux across different energy ranges across all pitch angles 0° to 180°: low-energy 6 eV - 1.4 keV (Figure 1g), mid-energy 1.8 - 27.5 keV (Figure 1h), high-energy 32 - 124 keV (Figure 1i) and 124 - 650 keV (Figure 1j). Initially, there is a higher differential energy flux (DEF) in the low-energy range (Figure 1g), with moderate fluxes in the mid (Figure 1h) and high-energy ranges (Figure 1i, j). However, these moderate and high energy fluxes get significantly intensified, termed as the high energy electron flux enhancement (Figure 1h, i, j). Omnidirectional DEF increases (Figure 1f) and is coincident with a decrease in the DEF of low-energy (Figure 1g) and an increase in the DEF of mid-energy (Figure 1h) and differential particle flux (DPF) of high-energy electrons (Figure 1i, j).

Electron-Scale Waves at High-Energy Flux Enhancement

We investigate the wave emissions during this high energy flux enhancement to examine whether the energetic electrons were produced locally by wave-particle interaction processes. Figures 2 and 3 show the simultaneous electron wave events observed during high-energy flux enhancement. Figure 2 illustrates the period from 14:46:54.882 UT to 14:46:56.882 UT. The frequency of the Hiss-like whistler band around 1 kHz, which is less than $0.5f_{ce}$ is identified from the electric and magnetic field spectrograms (Figure 2b, d). The wave normal angle is between 10° to 40°, indicating their quasi-parallel propagation (Figure 2e). The ellipticity is close to 1, implying their right-handed circular polarization (Figure 2f) that confirms the whistler wave. The electric field spectrogram shows a fundamental ECH band frequency around 4 kHz, with four harmonics at frequencies that are multiples of $(n+1)f_{ce}$, where n ranges from 1 to 4, extending up to electron plasma frequency, f_{pe} around 26 kHz (Figure 2b). The wave at f_{pe} is identified as the Langmuir wave by using the F_E index analysis proposed by Graham et al.³³, where F_E is the ratio of perpendicular power to total power in the snapshot, which is given by $F_E = \frac{\sum E_{\perp}^2}{\sum E_{\perp}^2 + \sum E_{\parallel}^2}$. For Langmuir waves, $F_E < 0.5$. For this case, $F_E = 0.092$ confirms that the observed wave is a Langmuir wave. Figure 2g shows an agyrotropy parameter³⁴ which quantifies the agyrotropy of electrons, measuring how much the electron velocity distribution deviates from gyrotyropy. The larger the Q value, the stronger the electron agyrotropy.

Another event of the simultaneous observation of whistler, ECH, and Langmuir waves from 14:47:12.537 UT to 14:47:16.416 UT is shown in Figure 3. The frequency of the whistler wave is approximately 1 kHz and is less than $0.5f_{ce}$ (Figure 3b, d), unlike the Hiss-like band, displays rising tones, aligning with intensifying magnetic field fluctuations (Figure 3c). The wave normal angle is around 10° (Figure 3e), and the ellipticity is close to 1 (Figure 3f). The electric field spectrogram shows both the fundamental band and the first harmonic of the ECH wave with frequencies 5 kHz and 10 kHz, corresponding to $(n+1)f_{ce}$, respectively (Figure 3b). The wave at frequency f_{pe} , around 25 kHz is identified as a Langmuir wave as the F_E index obtained here is 0.1³³ (Figure 3b). Figure 3g shows the gyrotopropy parameter during the wave event 2 (Figure 2g).

During this electron flux intensification, 16 bursts were observed in electric and magnetic field datasets. Among these, 8 bursts observed simultaneous wave activity of whistler waves, ECH waves, and Langmuir waves; 4 bursts showed simultaneous ECH waves and Langmuir waves; 1 burst contained both whistler and ECH waves, and 1 burst contained only ECH wave.

Generation Mechanism of the Waves

The observed electron distributions in the parallel and perpendicular directions are fitted using a subtracted bi-Maxwellian distribution with loss cone parameters (Figure 4a) (refer to the Electron Velocity Distribution Functions in the Methods section). These fitting parameters are given in Table 1. They were then used as input to the dispersion solver KUPDAP (Kyoto University Plasma Dispersion Analysis Package)³⁵ to analyze the growth of the instabilities (refer to the Linear Dispersion Analysis in the Methods section). For wave event 1 (Figure 2), the growth of the ECH wave and whistler wave is observed at 89.7° and 10° , respectively (Figure 4b, c). The growth of the fundamental band of waves around the f_{ce} and for harmonics around $(n+1)f_{ce}$, as well as the Langmuir waves is seen around 27 kHz (Figure 4b). This is in close agreement with the observed results. This analysis concludes that the observed background plasma conditions support the growth of instabilities that drive the observed electron-scale waves. This hints that the waves are locally generated by the electron loss cone distribution and their simultaneous occurrence is also verified using linear dispersion analysis. A similar analysis to check the growth of the instabilities is done for wave event 2 (Figure 3). This case also shows the growth of the whistler wave at 10° and ECH waves at 89.7° , which is not shown here.

Discussion

Although energetic electrons up to 125 keV have been observed at the magnetopause, such observations have not been observed frequently¹²⁻¹⁴. The statistical study of 250 magnetopause crossing of MMS shows either a direct or indirect connection between energetic electron enhancement and reconnection¹⁴. Whistler waves and energetic electrons are believed to be frequent outcomes of magnetic reconnection. However, more than half of the events in the statistical study observed energetic electrons without the occurrence of whistler waves¹⁴.

We report here the energetic electron flux enhancement up to 650 keV, which has no link to magnetic reconnection. In addition to whistler waves, the energetic electron flux event reported here exhibits Langmuir waves and ECH waves. Such a simultaneous observation of whistler waves, Langmuir waves, and ECH waves along with the prolonged electron flux enhancement near the Earth's magnetopause crossing has never been reported. These observations demonstrate the direct association of electron flux enhancement with the observed electron-scale waves.

The energy exchange parameter $\vec{J} \cdot \vec{E}$ is computed for wave event 1, i.e. (Figure 2), and positive values for the whistler wave (0.0120 nW/m³), the fundamental band of the ECH wave (0.1781 nW/m³), and the Langmuir wave (0.0004 nW/m³) are obtained as shown in the Supplementary Figure 3. This indicates a wave-particle interaction, suggesting that the electron-scale waves are transferring energy to the electrons³⁶ (refer to the Energy Transfer Parameter in Methods section). The electric field power of these waves is 1919 (mV/m)², 19343 (mV/m)², and 26.43 (mV/m)², respectively, highlighting the ECH wave may play a dominant role in energy exchange.

Our observations address two questions raised by Graham et al.³³: what instabilities generate waves around f_{pe} and do these waves contribute to plasma heating at magnetopause? The electron loss cone distribution functions, that drive electron-scale instabilities, are found simultaneously with the electron flux enhancement. Temperature anisotropy and the loss cone electron distributions observed at the magnetopause are likely to be the source of whistler waves, electron cyclotron harmonics waves, and Langmuir waves. The linear kinetic dispersion analysis shows that loss cone particle distribution provides a free energy source to excite these electron-scale instabilities that drive the respective wave. The observed high energetic electron flux event demonstrates the results of a cascading of all the possible effects via whistler waves, electron cyclotron harmonic waves and Langmuir waves. It is difficult to reveal the quantitative effects of each observed wave separately from the data. Further numerical simulations using particle-in-cell models are needed to quantify the systematic combined effects of whistler, electron cyclotron, and Langmuir waves from linear to nonlinear stages. Such a simulation would bring out the crucial role of cascading wave-particle interaction in understanding the electron energization and prolonged flux enhancement at the magnetopause, which has large-scale implications in near-Earth space.

Methods

Electron Velocity Distribution Functions

We fit the observed electron distributions (Figure 4a) by the subtracted bi-Maxwellian equation:

$$f(v_{\parallel}, v_{\perp}) = \frac{n}{\pi^{3/2} v_{\text{th}\parallel} v_{\text{th}\perp}^2} \exp\left(-\frac{(v_{\parallel} - v_d)^2}{v_{\text{th}\parallel}^2}\right) \left\{ \Delta \exp\left(-\frac{v_{\perp}^2}{v_{\text{th}\perp}^2}\right) + \frac{1 - \Delta}{1 - \beta} \left[\exp\left(-\frac{v_{\perp}^2}{v_{\text{th}\perp}^2}\right) - \exp\left(-\frac{v_{\perp}^2}{\beta v_{\text{th}\perp}^2}\right) \right] \right\} \quad (1)$$

where, $v_{\text{th}\parallel}$ and $v_{\text{th}\perp}$ are the parallel and perpendicular thermal velocities respectively calculated using the parallel and perpendicular temperature as $v_{\text{th}} = \sqrt{\frac{2kT}{m_e}}$. k is the Boltzmann constant, m_e is the electron mass, n is the density, v_d is the drift velocity, v_{\parallel} and v_{\perp} are the parallel and perpendicular velocity components, Δ and β are the loss cone parameters representing the loss cone depth and width, respectively.

The fitting parameters are given in Table 1. Only electron components from Table 1 are used to fit the observed velocity distribution (Figure 4a). The ion component is included to ensure plasma quasineutrality in KUPDAP. The drift velocity v_d is zero for all components.

Linear Dispersion Analysis

The fitting parameters in Table 1 are used in the Kyoto University Plasma Dispersion Analysis Package (KUPDAP) to investigate the growth of the instabilities. This Package is developed by the Space Group at the Kyoto University, Japan, is a tool for solving dispersion relations under the assumption of an infinite, uniform, collisionless plasma composed of multiple components, embedded in a consistent magnetic field³⁵. We use a loss cone distribution in the form of a subtracted bi-Maxwellian with loss cone parameters to model observed electron waves and assess whether the background plasma conditions support the growth of instabilities. In KUPDAP, the subtracted bi-Maxwellian distribution with loss cone parameters is applied to the anisotropic electron population, while all other electrons and ions are represented by a standard bi-Maxwellian distribution, which simplifies to a Maxwellian without any loss cone parameters.

Energy Transfer Parameter

The energy exchange within the waves and particles is quantified by $\vec{J} \cdot \vec{E}$, where \vec{E} represents the wave electric field and $\vec{J}(n_e, v_e)$ denotes turbulent electron currents generated. This parameter characterizes wave-particle interactions. The parameter $\vec{J} \cdot \vec{E}$ remains predominantly positive indicating the continuous energy transfer from the waves to the electrons and vice versa³⁶.

Data availability

MMS level-2 data analyzed in the present study are publicly available via the MMS Science Data Center (<https://lasp.colorado.edu/mms/sdc/public/>).

Code availability

The Kyoto University Plasma Dispersion Analysis Package (KUPDAP) that was used to calculate the dispersion relation of the electron-scale waves is available at <http://space.rish.kyoto-u.ac.jp/software>.

References

1. Frey, H., Phan, T., Fuselier, S. & Mende, S. Continuous magnetic reconnection at earth's magnetopause. *Nature* **426**, 533–537, DOI: <https://doi.org/10.1038/nature02084> (2003).
2. Hesse, M. & Cassak, P. Magnetic reconnection in the space sciences: Past, present, and future. *J. Geophys. Res. Space Phys.* **125**, e2018JA025935, DOI: <https://doi.org/10.1029/2018JA025935> (2020).
3. Hwang, K.-J. Magnetopause waves controlling the dynamics of earth's magnetosphere. *J. Astron. Space Sci.* **32**, 1–11, DOI: <https://doi.org/10.5140/JASS.2015.32.1.1> (2015).
4. Tang, X. *et al.* Themis observations of the magnetopause electron diffusion region: Large amplitude waves and heated electrons. *Geophys. Res. Lett.* **40**, 2884–2890, DOI: <https://doi.org/10.1002/grl.50565> (2013).
5. Øieroset, M., Lin, R., Phan, T., Larson, D. & Bale, S. Evidence for electron acceleration up to 300 keV in the magnetic reconnection diffusion region of earth's magnetotail. *Phys. Rev. Lett.* **89**, 195001, DOI: <https://doi.org/10.1103/PhysRevLett.89.195001> (2002).
6. Wang, R., Lu, Q., Li, X., Huang, C. & Wang, S. Observations of energetic electrons up to 200 keV associated with a secondary island near the center of an ion diffusion region: A cluster case study. *J. Geophys. Res. Space Phys.* **115**, DOI: <https://doi.org/10.1029/2010JA015473> (2010).

7. Zhang, X.-J. *et al.* Relativistic and ultra-relativistic electron bursts in earth's magnetotail observed by low-altitude satellites. *arXiv preprint arXiv:2408.17299* (2024).
8. Khotyaintsev, Y. V., Graham, D. B., Norgren, C. & Vaivads, A. Collisionless magnetic reconnection and waves: Progress review. *Front. Astron. Space Sci.* **6**, 70, DOI: <https://doi.org/10.3389/fspas.2019.00070> (2019).
9. Wei, X. *et al.* Cluster observations of waves in the whistler frequency range associated with magnetic reconnection in the earth's magnetotail. *J. Geophys. Res. Space Phys.* **112**, DOI: <https://doi.org/10.1029/2006JA011771> (2007).
10. Farrell, W., Desch, M., Kaiser, M. & Goetz, K. The dominance of electron plasma waves near a reconnection x-line region. *Geophys. research letters* **29**, 8–1, DOI: <https://doi.org/10.1029/2002GL014662> (2002).
11. Farrell, W., Desch, M., Ogilvie, K., Kaiser, M. & Goetz, K. The role of upper hybrid waves in magnetic reconnection. *Geophys. research letters* **30**, DOI: <https://doi.org/10.1029/2003GL017549> (2003).
12. Jaynes, A. *et al.* Energetic electron acceleration observed by mms in the vicinity of an x-line crossing. *Geophys. Res. Lett.* **43**, 7356–7363, DOI: <https://doi.org/10.1002/2016GL069206> (2016).
13. Fu, H. *et al.* Evidence of electron acceleration at a reconnecting magnetopause. *Geophys. Res. Lett.* **46**, 5645–5652, DOI: <https://doi.org/10.1029/2019GL083032> (2019).
14. Chepuri, S. N. *et al.* A statistical study of magnetopause boundary layer energetic electron enhancements using mms. *Front. astronomy space sciences* **9**, 926660, DOI: <https://doi.org/10.3389/fspas.2022.926660> (2022).
15. Contel, O. L. *et al.* Whistler mode waves and hall fields detected by mms during a dayside magnetopause crossing. *Geophys. Res. Lett.* **43**, 5943–5952, DOI: <https://doi.org/10.1002/2016GL068968> (2016).
16. Wilder, F. *et al.* Observations of whistler mode waves with nonlinear parallel electric fields near the dayside magnetic reconnection separatrix by the magnetospheric multiscale mission. *Geophys. Res. Lett.* **43**, 5909–5917, DOI: <https://doi.org/10.1002/2016GL069473> (2016).
17. Zhou, M. *et al.* Magnetospheric multiscale observations of an ion diffusion region with large guide field at the magnetopause: Current system, electron heating, and plasma waves. *J. Geophys. Res. Space Phys.* **123**, 1834–1852, DOI: <https://doi.org/10.1002/2017JA024517> (2018).
18. Zhou, M. *et al.* Observation of high-frequency electrostatic waves in the vicinity of the reconnection ion diffusion region by the spacecraft of the magnetospheric multiscale (mms) mission. *Geophys. Res. Lett.* **43**, 4808–4815, DOI: <https://doi.org/10.1002/2016GL069010> (2016).
19. Li, J. *et al.* Local excitation of whistler mode waves and associated langmuir waves at dayside reconnection regions. *Geophys. Res. Lett.* **45**, 8793–8802, DOI: <https://doi.org/10.1029/2018GL078287> (2018).
20. Yu, X. *et al.* Simultaneous observation of whistler waves and electron cyclotron harmonic waves in the separatrix region of magnetopause reconnection. *J. Geophys. Res. Space Phys.* **126**, e2021JA029609, DOI: <https://doi.org/10.1029/2021JA029609> (2021).
21. Peng, Q. *et al.* Variation of dayside chorus waves associated with solar wind dynamic pressure based on mms observations. *Adv. Space Res.* **65**, 2551–2558, DOI: <https://doi.org/10.1016/j.asr.2020.03.006> (2020).
22. Meredith, N. P., Horne, R. B., Thorne, R. M. & Anderson, R. R. Survey of upper band chorus and ech waves: Implications for the diffuse aurora. *J. Geophys. Res. Space Phys.* **114**, DOI: <https://doi.org/10.1029/2009JA014230> (2009).
23. Ni, B., Gu, X., Fu, S., Xiang, Z. & Lou, Y. A statistical survey of electrostatic electron cyclotron harmonic waves based on themis fff wave data. *J. Geophys. Res. Space Phys.* **122**, 3342–3353, DOI: <https://doi.org/10.1002/2016JA023433> (2017).
24. Liu, X., Chen, L., Engel, M. A. & Jordanova, V. K. Global simulation of electron cyclotron harmonic wave instability in a storm-time magnetosphere. *Geophys. Res. Lett.* **47**, e2019GL086368, DOI: <https://doi.org/10.1029/2019GL086368> (2020).
25. Xie, Y. *et al.* Interplanetary shock induced intensification of electron cyclotron harmonic waves in the earth's inner magnetosphere. *Front. Phys.* **12**, 1334531, DOI: <https://doi.org/10.3389/fphy.2024.1334531> (2024).
26. Burch, J., Moore, T., Torbert, R. & Giles, B.-h. Magnetospheric multiscale overview and science objectives. *Space Sci. Rev.* **199**, 5–21, DOI: <https://doi.org/10.1007/s11214-015-0164-9> (2016).
27. Ergun, R. *et al.* The axial double probe and fields signal processing for the mms mission. *Space Sci. Rev.* **199**, 167–188, DOI: <https://doi.org/10.1007/s11214-014-0115-x> (2016).
28. Lindqvist, P.-A. *et al.* The spin-plane double probe electric field instrument for mms. *Space Sci. Rev.* **199**, 137–165, DOI: <https://doi.org/10.1007/s11214-014-0116-9> (2016).

29. Russell, C. *et al.* The magnetospheric multiscale magnetometers. *Space Sci. Rev.* **199**, 189–256, DOI: <https://doi.org/10.1007/s11214-014-0057-3> (2016).
30. Le Contel, O. *et al.* The search-coil magnetometer for mms. *Space Sci. Rev.* **199**, 257–282, DOI: <https://doi.org/10.1007/s11214-014-0096-9> (2016).
31. Pollock, C. *et al.* Fast plasma investigation for magnetospheric multiscale. *Space Sci. Rev.* **199**, 331–406, DOI: <https://doi.org/10.1007/s11214-016-0245-4> (2016).
32. Blake, J. *et al.* The fly’s eye energetic particle spectrometer (feeps) sensors for the magnetospheric multiscale (mms) mission. *Space Sci. Rev.* **199**, 309–329, DOI: <https://doi.org/10.1007/s11214-015-0163-x> (2016).
33. Graham, D. B. *et al.* Large-amplitude high-frequency waves at earth’s magnetopause. *J. Geophys. Res. Space Phys.* **123**, 2630–2657, DOI: <https://doi.org/10.1002/2017JA025034> (2018).
34. Swisdak, M. Quantifying gyrotropy in magnetic reconnection. *Geophys. Res. Lett.* **43**, 43–49, DOI: <https://doi.org/10.1002/2015GL066980> (2016).
35. Sugiyama, H. *et al.* Electromagnetic ion cyclotron waves in the earth’s magnetosphere with a kappa-maxwellian particle distribution. *J. Geophys. Res. Space Phys.* **120**, 8426–8439, DOI: <https://doi.org/10.1002/2015JA021346> (2015).
36. Liu, C. *et al.* Ultrafast measurement of field-particle energy transfer during chorus emissions in space. *arXiv preprint arXiv:2408.13156* (2024).

Acknowledgments

We thank the MMS Science Data Center (<https://lasp.colorado.edu/mms/sdc/public/>) for providing the data for this study. The authors thank the entire MMS team and instrument PIs for data access and support. S.L., A.K., and B.K. acknowledge support from IIG for research funding under the MI-PEARL project.

Author contributions statement

A.K. designed the study and oversaw the project. S.L. carried out the data analysis under the supervision of A.K. and prepared the initial draft of the manuscript. A.K. and B.K. contributed to the data interpretation and edited the manuscript.

Competing interests

The authors declare no competing interests.

Components	n (cm ⁻³)	T_{\parallel} (eV)	T_{\perp} (eV)	Δ	β
1. Electron	15	5	5	0	0
2. Electron	10.5	184	184	0	0
3. Electron	1	500	500	0	0
4. Electron	0.3	2000	3200	1	0.2
5. Electron	0.05	1.95×10^4	1.95×10^4	0	0
6. Proton	26.85	2000	2000	0	0

Table 1. Plasma parameters used in fitting the observed electron distribution shown in Figure 4a

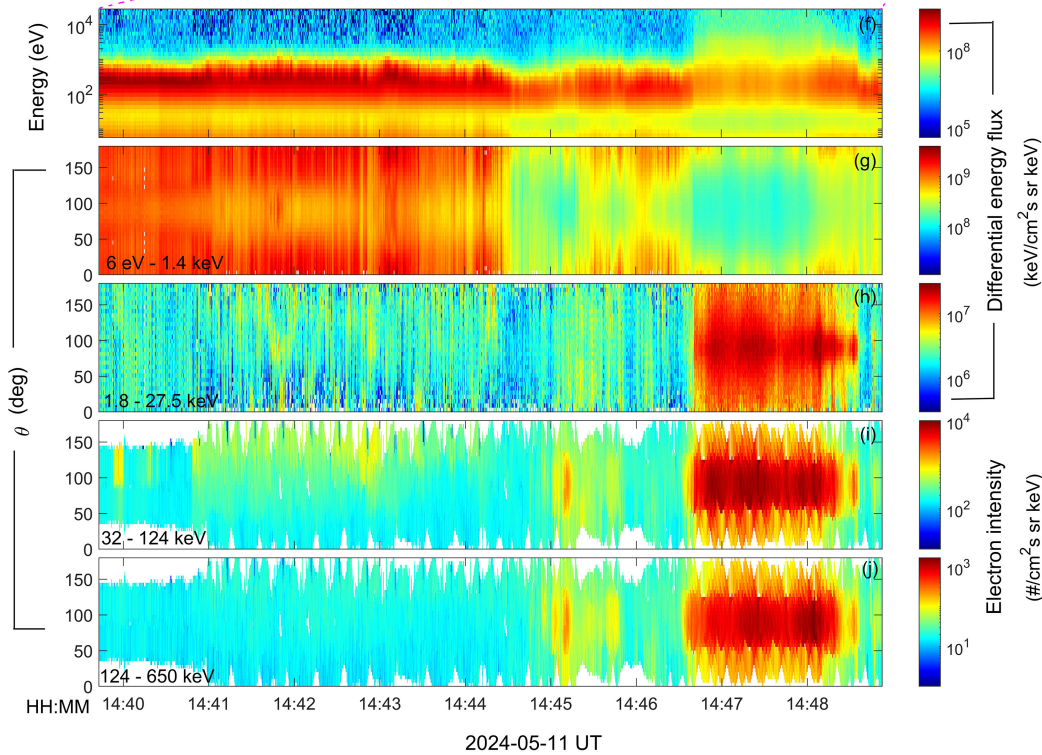
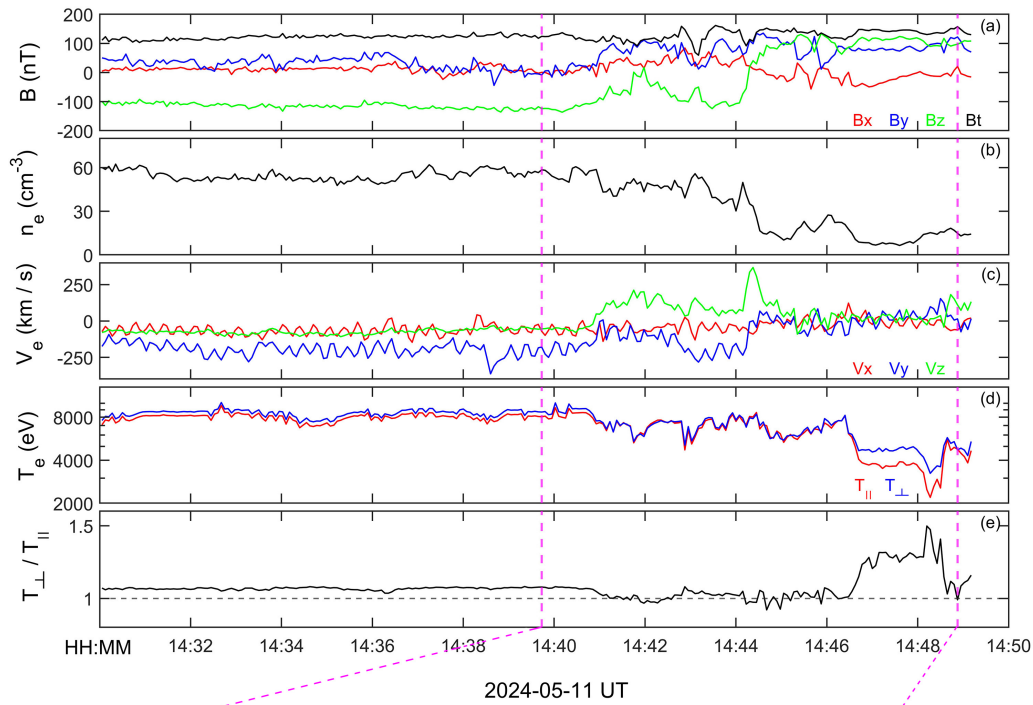


Figure 1. MMS parameters: (a) Magnetic field in GSE coordinate system, (b) Electron density, (c) Electron velocity, (d) Electron temperature for energy range 1 keV to 27.5 keV, (e) Temperature anisotropy for 1 keV to 27.5 keV. Magenta dashed lines indicate the availability of the burst mode dataset, (f) Electron omnidirectional energy spectrogram, (g) Pitch angle distribution of 6 eV - 1.4 keV electrons, (h) Pitch angle distribution of 1.8 - 27.5 keV electrons, (i) Pitch angle distribution of 32 - 124 keV electrons, (j) Pitch angle distribution of 124 - 650 keV electrons.

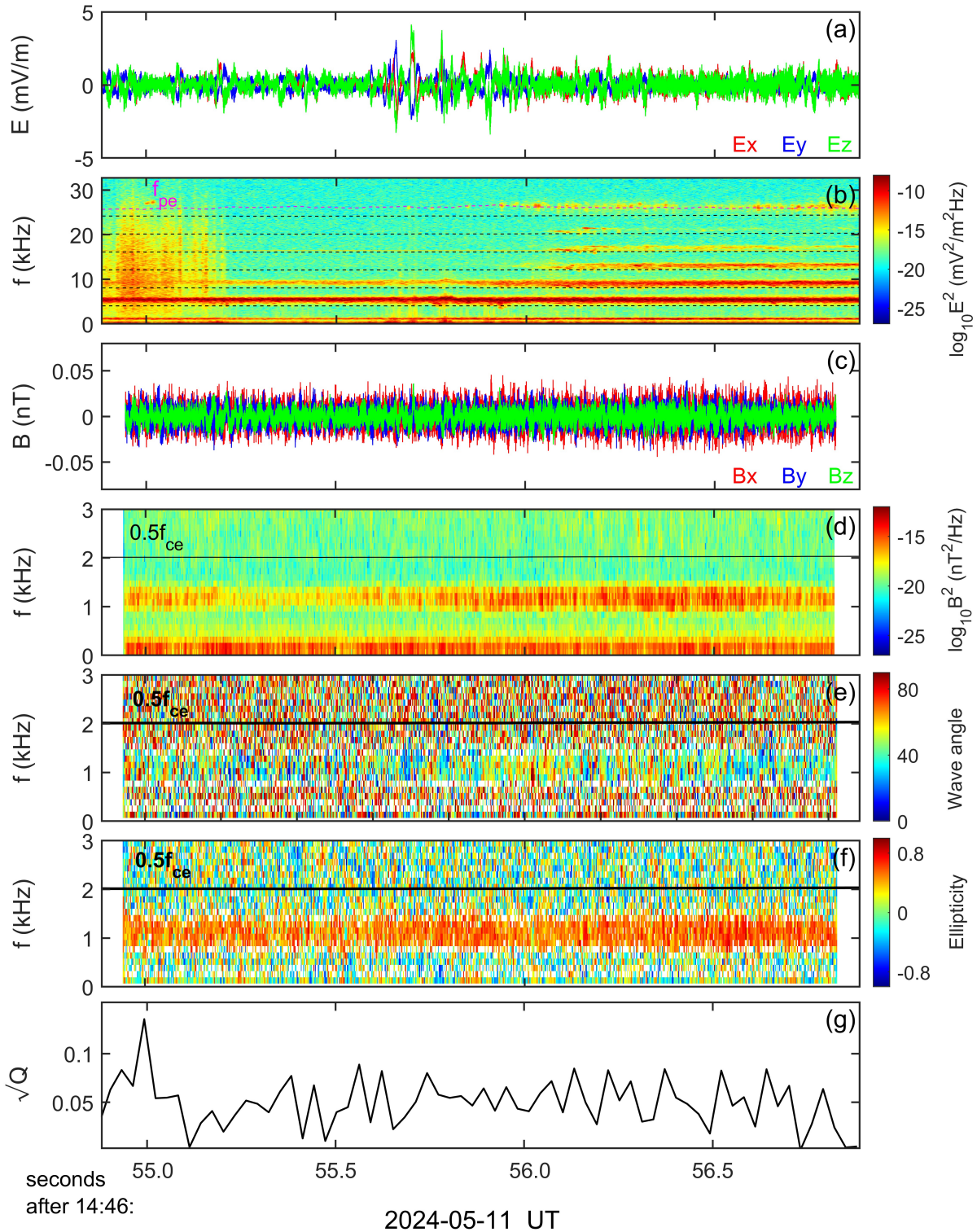


Figure 2. Wave event 1: Simultaneous observation of whistler wave, electron cyclotron harmonics (ECH), and Langmuir wave: (a) Electric field in GSE coordinate system, (b) Electric field spectrogram (black and magenta dashed lines represent $n f_{ce}$, where $n = 1$ to 6 and f_{pe} respectively), (c) Magnetic field in GSE coordinate system, (d) Magnetic field spectrogram, (e) Wave normal angle of whistler wave, (f) Ellipticity of whistler wave (solid black lines in panel d, e, f represent $0.5 f_{ce}$), (g) Agyrotropy parameter for 1 keV to 27.5 keV electrons.

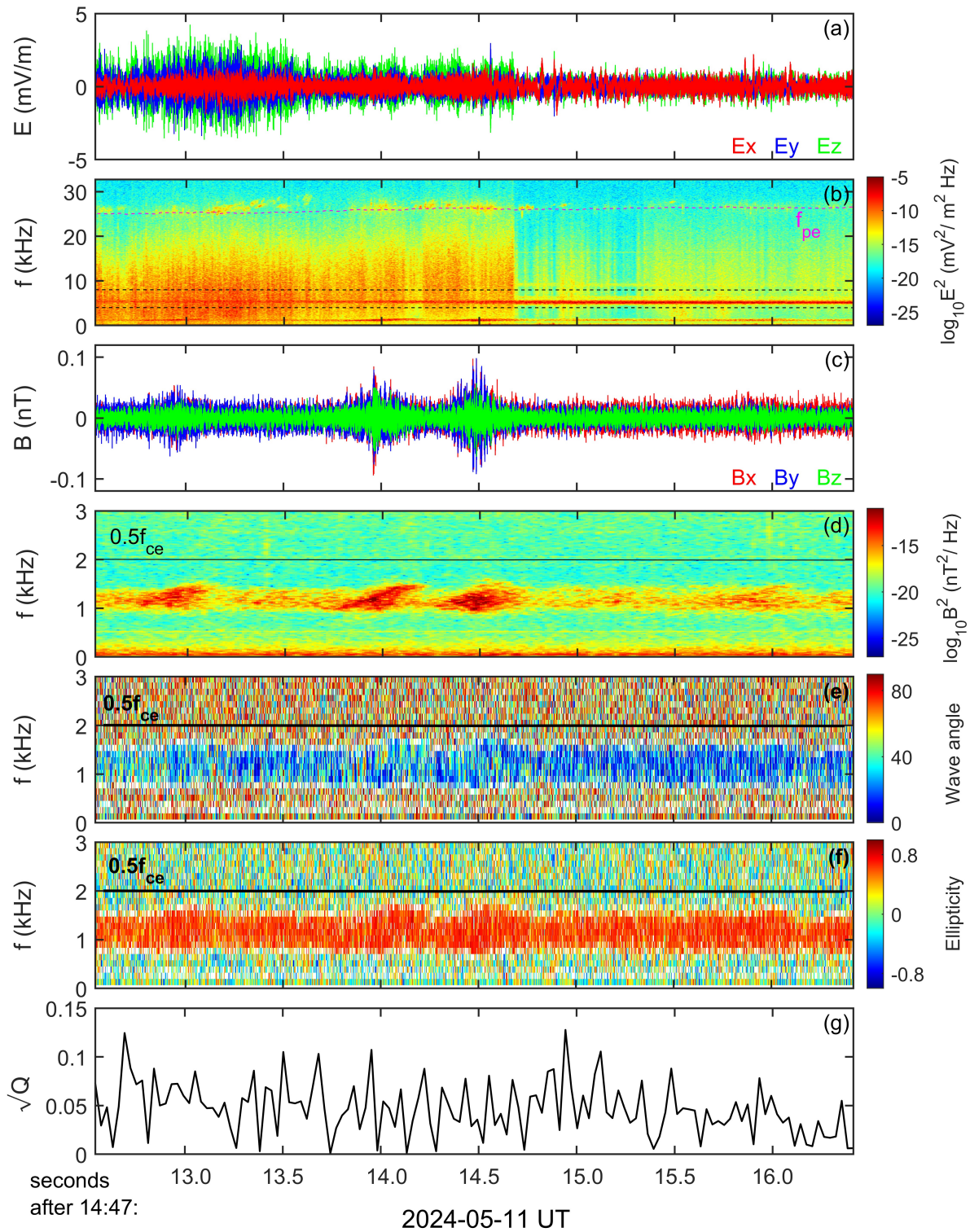


Figure 3. Wave event 2: Simultaneous observation of whistler wave, electron cyclotron harmonics (ECH), and Langmuir wave: (a) Electric field in GSE coordinate system, (b) Electric field spectrogram (black and magenta dashed lines represent $n f_{ce}$, where $n = 1, 2$ and f_{pe} respectively), (c) Magnetic field in GSE coordinate system, (d) Magnetic field spectrogram, (e) Wave normal angle of whistler wave, (f) Ellipticity of whistler wave (solid black lines in panel d, e, f represent $0.5 f_{ce}$), (g) Agyrotropy parameter for 1 keV to 27.5 keV electrons.

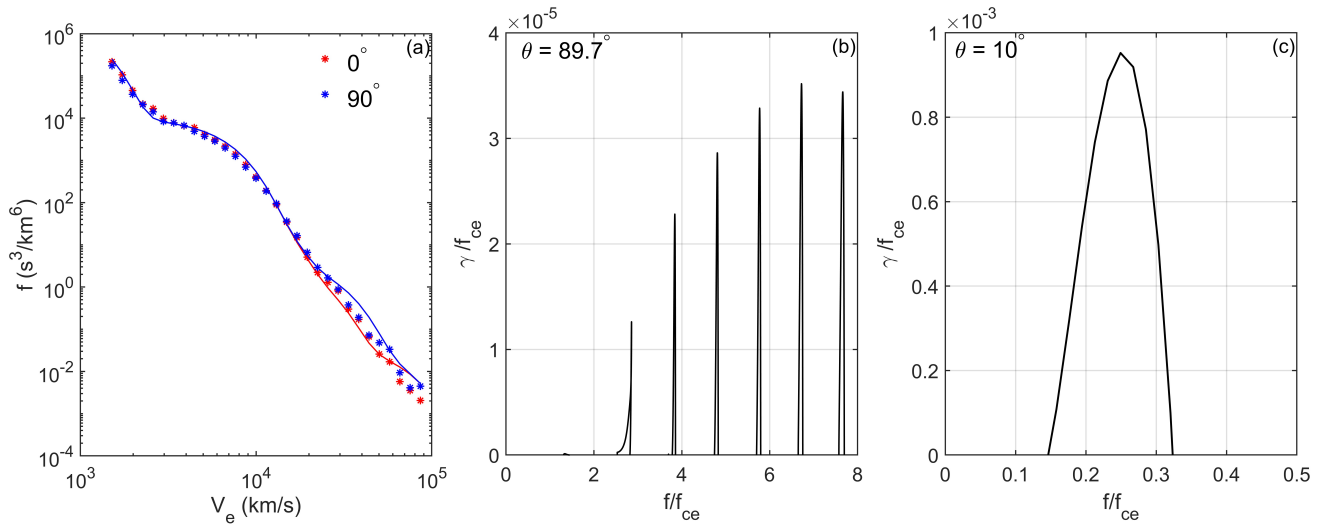
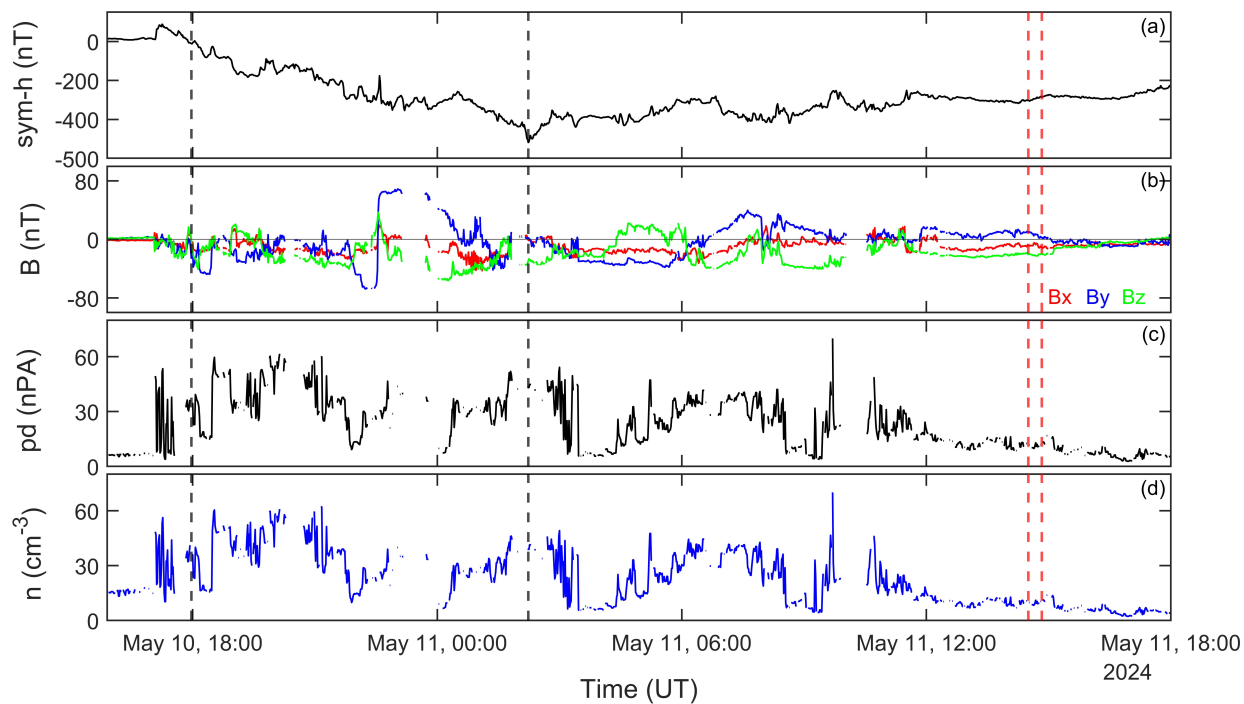


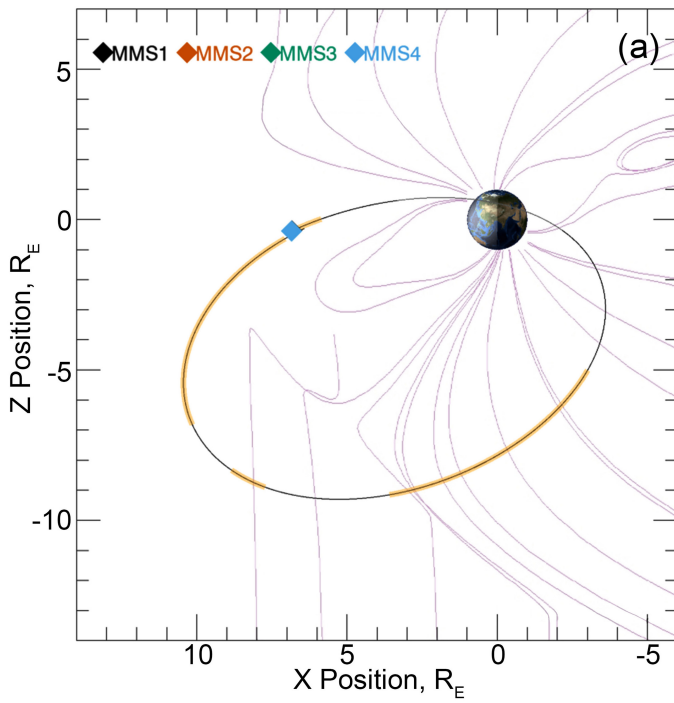
Figure 4. The electron distributions and growth rates for wave event 1: (a) Electron phase space density vs electron velocity in parallel and perpendicular directions with red and blue representing 0° and 90° respectively, at 14:46:55.682 UT, (b) The growth rate of ECH and Langmuir wave at 89.7° , (c) The growth rate of whistler wave at 10° .

Supplementary information

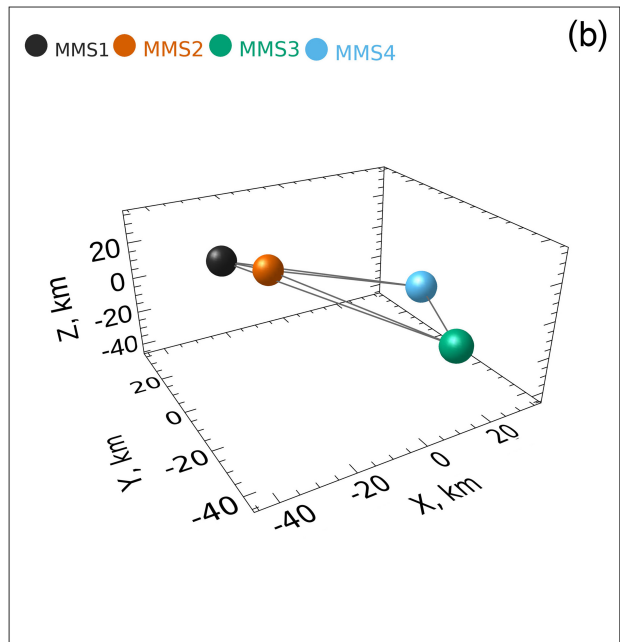


Supplementary Figure 1: The strongest storm of two decades is recorded in OMNI data: (a) SYM-H, (b) Interplanetary magnetic field in GSE coordinate system, (c) Solar wind dynamic pressure, (d) Proton density. Black dashed lines indicate the timestamps corresponding to the storm's main phase and red dashed lines indicate the Magnetospheric Multiscale (MMS) satellites were at the magnetopause.

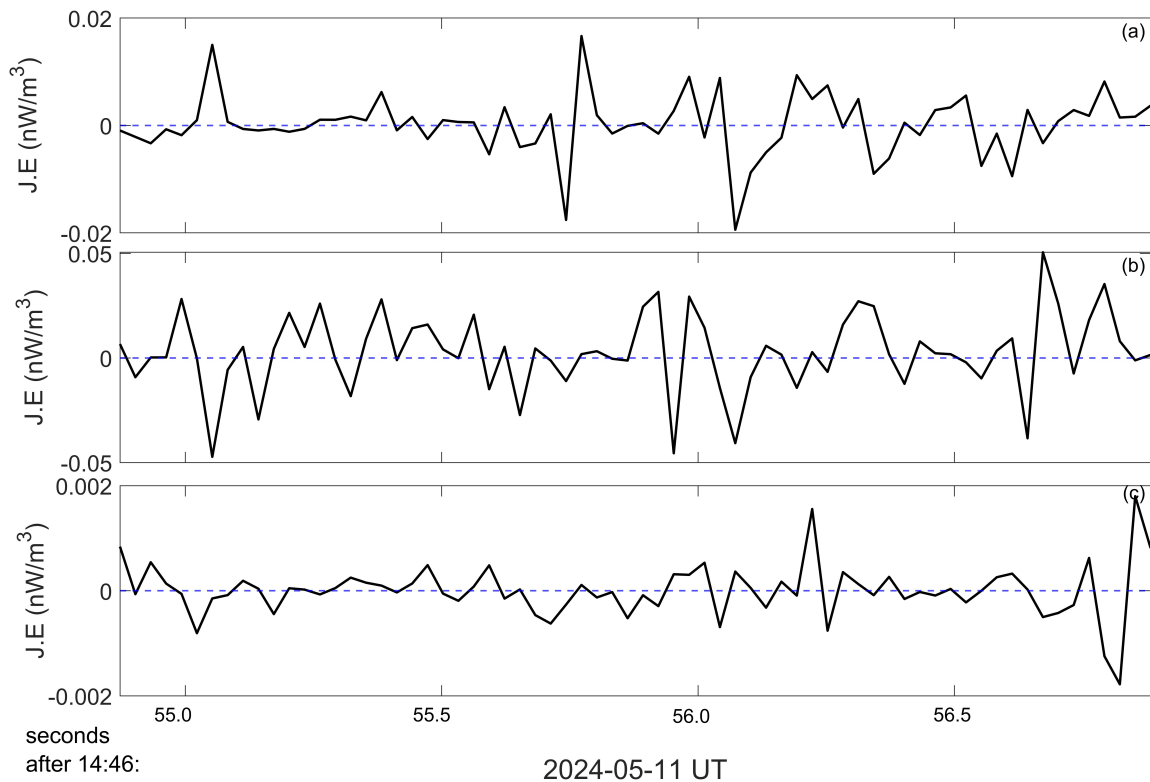
MMS Formation 2024-05-11 14:00:00 UT



MMS Formation 2024-05-11 14:47:00 UT



Supplementary Figure 2: MMS parameters: (a) MMS around magnetopause, orbiting towards Earth, (b) Tetrahedral geometry of all MMS satellites.



Supplementary Figure 3: Energy transfer parameter $\vec{J} \cdot \vec{E}$ for: (a) Whistler wave, (b) Fundamental band of ECH wave, (c) Langmuir wave.